Identification of sources of potential fields with the continuous wavelet transform: Two-dimensional ridgelet analysis

Hassina Boukerbout, Dominique Gibert

Identification of sources of potential fields with the continuous wavelet transform: Two-dimensional ridgelet analysis

Hassina Boukerbout[1,2] and Dominique Gibert[3]

Received 30 September 2005; revised 27 February 2006; accepted 6 March 2006; published 19 July 2006.

[1] A method based on the wavelet transform is used to localize the causative sources of potential field anomalies. In previous studies we introduced a particular class of analyzing wavelets belonging to the Poisson semigroup and such that the analyzed anomaly has a conical signature in the wavelet domain with its apex pointing at the location of the causative homogeneous source. In the present paper we apply this formalism to the special case of anomalies produced by elongated sources like faults and dikes. We show that, for this particular type of anomalies, the two-dimensional (2-D) wavelet transform corresponds to the ridgelet analysis and reduces to the 1-D wavelet transform applied in the Radon domain. A complete synthetic example is used to illustrate all steps of the analysis method: Radon transform of the anomaly map, selection of the Radon signature of elongated anomalies, complex wavelet transform, and source localization with the conical signature in the wavelet domain. The azimuthal filtering performed in the Radon domain leads to high signal-to-noise ratio and good localization of the sources both horizontally and vertically. The synthetic example is completed by an application of the method to a real aeromagnetic survey acquired in Britanny (France) and the results are compared with source depth determinations made with the Euler deconvolution method.

Citation: Boukerbout, H., and D. Gibert (2006), Identification of sources of potential fields with the continuous wavelet transform: Two-dimensional ridgelet analysis, *J. Geophys. Res.*, *111*, B07104, doi:10.1029/2005JB004078.

1. Introduction

[2] The characterization and the localization of the sources of geophysical potential fields (electrical, magnetic, gravitational, thermal, etc.) measured at the surface of the Earth continues to motivate numerous methodological studies resulting in a number of inversion and analysis techniques [e.g., *Blakely*, 1996]. Inversion methods are aimed at recovering the source distribution by inverting an integral equation linking the source distribution to the measured potential field [e.g., *Cuer and Bayer*, 1980; *Tarantola*, 1987; *Parker*, 1994; *Li and Oldenburg*, 1996], leading to more or less sophisticated algorithms depending on their ability to tackle with geological prior constrains to reduce nonuniqueness [*Pilkington*, 1997; *Bosch et al.*, 2001]. Analyzing methods, which do not belong to the inverse-methods family defined above, do not necessarily directly look for the source distribution but, instead, bring the information carried by the measured field in dual spaces where things may, hopefully, become easier to understand. For instance, the dual target space is the Fourier domain where the information is statistically processed to give clues to the depth to top of the causative sources [*Spector and Grant*, 1970; *Green*, 1972].

[3] Other analyzing methods are the well-known transformation techniques like downward continuation, reduction to the pole and oblique derivatives which produce transformed fields, ϕ_T, where features of the original field, ϕ_0, are enhanced [*Paul et al.*, 1966; *Bhattacharyya*, 1972; *Baranov*, 1975; *Gibert and Galdéano*, 1985; *Sowerbutts*, 1987; *Pilkington et al.*, 1994]. In symbolic form, this reads

$$\phi_T = \mathcal{O}_1 * \ldots * \mathcal{O}_N * \phi_0, \tag{1}$$

where the asterisk stands for convolution over the horizontal plane, and $\mathcal{O}_i$ represents various transformation operators. The relationship between the measured field $\phi_0(\mathbf{h}, z)$ and the distribution of its sources, $s(\mathbf{h}, z)$, may be written as a sum of convolution products,

$$\phi_0(\mathbf{h}) = \int_{-\infty}^{0} \mathrm{d}z[s(\cdot, z) * G(\cdot, z)](\mathbf{h}), \tag{2}$$

where $G(\mathbf{h}, z)$ is a suitable Green function, and $\mathbf{h}$ is the horizontal vector representing the position in the horizontal plane. Inserting this expression into (1), we obtain

$$\phi_T(\mathbf{h}) = \int_{-\infty}^{0} \mathrm{d}z\mathcal{O}_1 * \ldots * \mathcal{O}_N * [s(\cdot, z) * G(\cdot, z)](\mathbf{h}). \tag{3}$$

[1] Centre de Recherche en Astronomie, Astrophysique and Géophysique, Observatoire d'Alger, Algeria.
[2] Formerly at Géosciences Rennes, Rennes, France.
[3] Géosciences Rennes, CNRS/INSU (UMR 6118) and Université Rennes 1, Rennes, France.

0148-0227/06/2005JB004078$09.00

[4] Most transformation operators $\mathcal{O}_i$ are derived in the framework of potential field theory, and their action makes sense only with respect to potential fields whose partial derivatives are linked through the Laplace equation. Such is the case of the continuation operators which act along the vertical direction, z, through a convolution restricted to the horizontal plane. However, the action of some operators keeps its sense even when applied to functions which are not potential fields. This is the case of the operators acting as combinations of horizontal derivatives which may be applied to the source function $s(\mathbf{h}, z)$ without loosing their physical sense. If a number $M \leq N$ of such operators are present in the transformation equation (3), their actions may be decoupled from those of the remaining operators and equation (3) may be rewritten as

$$\phi_T(\mathbf{h}) = \mathcal{O}_\phi * \int_{-\infty}^{0} \mathrm{d}z[s_T(\cdot, z) * G(\cdot, z)](\mathbf{h}), \tag{4}$$

where $\mathcal{O}_\phi$ represents the $N - M$ operators whose actions are limited to potential fields, and

$$s_T = \mathcal{O}_1 * \ldots * \mathcal{O}_M * s(\cdot, z) \tag{5}$$

represents the transformed source distribution obtained by applying the M operators $\mathcal{O}_1, \ldots, \mathcal{O}_M$ to the initial source function s.

[5] Owing to equation (4), the transformed field ϕ_T may now be seen as being produced by the transformed sources s_T. This is one of the main properties which make the transformation methods so useful to localize the edges of the sources of the measured field. For instance, assuming that the causative sources are prismatic bodies with constant parameters (density, magnetization, etc.) and applying a simple horizontal derivative operator we get a transformed source function s_T which vanishes everywhere excepted at the edges of the prismatic bodies where the relevant physical parameters display abrupt changes in the direction of the applied horizontal derivative. Consequently, the transformed field ϕ_T may be interpreted as being the field produced by localized sources (possibly positive or negative) restricted to the edges of the prisms.

[6] Because of the sparsity of the transformed source function whose support is limited to the disjoint edges of the source bodies, the anomalies of the transformed field often decoalesce, enabling an easier localization of the limits of the source units. This, however, does not allow to localize the sources along the vertical dimension as easily as for the horizontal dimensions, and the depth to the source must be determined by analyzing the whole shape of the anomalies. This approach may be traced back to the graphical methods where the depth of the sources is obtained from remarkable geometrical features of the anomalies like horizontal distances between half-width maximum, inflexion points and so on [e.g., *Dobrin and Savit*, 1988]. A general mathematical framework may be constructed from the homogeneity properties of the potential field anomalies produced by homogeneous point sources like monopoles, dipoles, etc. To our knowledge, these properties were first used in geophysics by *Negi* [1967] and *Roy* [1967] who linked the divergence rate of downward continuation to the depth of the causative sources. A more systematic approach, based on the discrepancy between analytical continuation and truncated series developments, was subsequently proposed by *Galdéano* [1974]. A local-analysis method, also based on the shape of anomalies, is the Euler deconvolution [*Thompson*, 1982] which however needs regularization and filtering to eliminate strong noise effects [e.g., *Mikhailov et al.*, 2003].

[7] The wavelet approach independently proposed by *Moreau et al.* [1997] and *Hornby et al.* [1999] also exploits the homogeneity properties of the potential field to both detect, localize and characterize the sources. Further developments [*Moreau et al.*, 1999; *Sailhac and Gibert*, 2003] revealed that the wavelet approach is particularly efficient to deal with noise as shown through applications to aeromagnetic data [*Sailhac et al.*, 2000; *Boschetti et al.*, 2004], spontaneous electrical potential [*Gibert and Pessel*, 2001; *Sailhac and Marquis*, 2001], gravity data [*Martelet et al.*, 2001; *Fedi et al.*, 2004], and electromagnetic data [*Boukerbout et al.*, 2003]. Further work remains to be done to develop the 2-D wavelet method in order to account for the variety of shapes of the potential field anomalies which may be encountered in practice. In the present study, we consider the special case of elongated anomalies produced by geological features like dikes and faults. This particular class of anomalies may be efficiently analyzed with a special form of the wavelet analysis based on the use of the so-called ridgelet functions [*Candès*, 1998]. We first recall the basics of the wavelet analysis of potential fields. Next, we show how the method may be extended to the 2-D case and how ridgelet functions may be used to analyze anomalies caused by elongated source distributions. Finally, we present and discuss an application to a part of the aeromagnetic survey of Brittany, France.

2. Ridgelet Transform of Potential Field Anomalies

[8] In this section we recall the main mathematical background necessary to make the paper self-consistent. A general presentation of the wavelet theory may be found in the book by *Holschneider* [1995] and a detailed discussion of the wavelet transform applied to potential field theory is given by *Moreau et al.* [1997, 1999], *Sailhac et al.* [2000], and *Sailhac and Gibert* [2003]. We only write the equations for both the 1-D and 2-D cases relevant in the present study, and we use the same mathematical notations as in the paper by *Sailhac and Gibert* [2003] where further developments for the 2-D case may be found.

2.1. The 1-D Continuous Wavelet Transform

[9] We define the 1-D continuous wavelet transform, $\mathcal{W}[g, \phi_0]$ (b, a), of a function $\phi_0(x \in \mathrm{R})$ as the convolution product,

$$\begin{aligned}\mathcal{W}[g, \phi_0](b, a) &\equiv \int_{\mathrm{R}} \frac{1}{a} g\left(\frac{b - x}{a}\right) \phi_0(x) \mathrm{d}x \\ &= (\mathcal{D}_a g * \phi_0)(b),\end{aligned} \tag{6}$$

where the function $g(x)$ is called the analyzing wavelet, $a \in \mathrm{R}^+$ is the dilation parameter, b is the translation parameter,

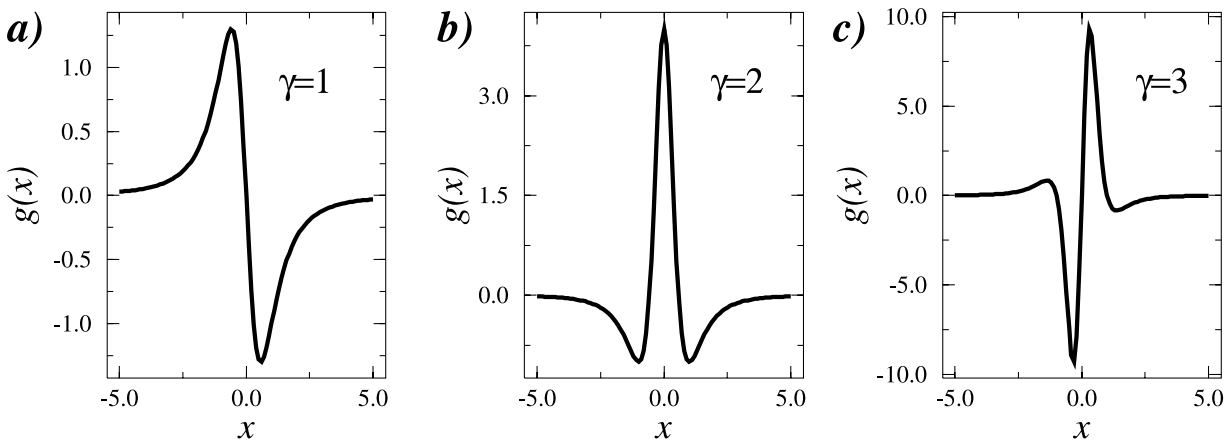

Figure 1. Analyzing wavelets g belonging to the Poisson semigroup and corresponding to increasing γ values. Convolution with these wavelets mainly acts as an horizontal derivative of order γ combined with an upward continuation with an offset Δz proportional to dilation a. The wavelets are given by $g(x) = -(\frac{2}{\pi})x(1 + x^2)^{-2}$, $g(x) = -(\frac{2}{\pi})(1 - 3x^2)(1 + x^2)^{-3}$, and $g(x) = (\frac{24}{\pi})(1 - x^2)(1 + x^2)^{-4}$ from left to right.

and the dilation operator $\mathcal{D}_a$ is defined by the following action [*Goupillaud et al.*, 1984]:

$$\mathcal{D}_a g(x) \equiv \frac{1}{a} g\left(\frac{x}{a}\right). \tag{7}$$

To be an admissible analyzing wavelet the function g must belong to the class of the zero-mean oscillating functions with a compact (or quasicompact) support restricted to a finite interval $\mathcal{S}_x$ containing the origin [*Holschneider*, 1995]. The analyzing wavelet is therefore a bandpass filter. Several wavelets are shown in Figure 1.

[10] The wavelet transform possesses many nice mathematical properties, and, in the present study, we are particularly interested by the properties of the wavelet transform with respect to homogeneous functions. The fundamental formula we need is the covariance of the wavelet transform with respect to a dilation $\lambda > 0$ of the transformed function,

$$\mathcal{W}[g, \mathcal{D}_\lambda \phi_0](b, a) = \frac{1}{\lambda} \mathcal{W}[g, \phi_0]\left(\frac{b}{\lambda}, \frac{a}{\lambda}\right). \tag{8}$$

The geometrical meaning of this equation is that the wavelet transform of a dilated function, $\mathcal{D}_\lambda \phi_0$, is the wavelet transform of the nondilated function ϕ_0 rescaled on both the a and b axes. We now consider the particular class of the homogeneous functions such that their dilated versions verify

$$\phi_0(\lambda x) = \lambda^\alpha \phi_0(x), \tag{9}$$

where $\alpha \in \mathrm{R}$ is the homogeneity degree. An homogeneous function is such that its appearance remains unchanged when the function is observed at different scales. The homogeneity degree controls the aspect ratio between the horizontal and the vertical scales. For such a function, equation (8) simplifies to

$$\mathcal{W}[g, \phi_0](\lambda b, \lambda a) = \lambda^\alpha \mathcal{W}[g, \phi_0](b, a). \tag{10}$$

The important result brought by equation (10) is that the entire wavelet transform of a homogeneous function can be obtained from the wavelet transform taken at a single dilation:

$$\mathcal{W}[g, \phi_0](b, a') = \left(\frac{a'}{a}\right)^{1+\alpha} \mathcal{D}_{a'/a} \mathcal{W}[g, \phi_0](b, a), \tag{11}$$

where the dilation operator is understood to act on the translation variable b only. The geometrical sense of this equation is that the wavelet transform of a homogeneous singularity has the appearance of a cone whose apex points onto the singularity for $a \downarrow 0^+$ (Figure 2). As can be observed, the amplitude of the wavelet transform is controlled by the homogeneity degree of the analyzed function. This property is at the basis of the wavelet method used to detect and characterize homogeneous singularities in signals [*Grossmann et al.*, 1987; *Holschneider*, 1988; *Mallat and Hwang*, 1992]. A detailed discussion of this technique and applications to geomagnetic time series can be found in the papers by *Alexandrescu et al.* [1995, 1996]. Further applications of this method to the characterization of seismic interfaces are given by *Le Gonidec et al.* [2002, 2003].

2.2. Poisson Wavelets

[11] Previous studies [*Moreau et al.*, 1997, 1999; *Sailhac et al.*, 2000; *Sailhac and Gibert*, 2003] demonstrated that when applied to potential fields, the wavelet transform can be given a deep physical sense. The main physical principle at the basis of our method is to observe that the potential field caused by a homogeneous source like a monopole, a dipole, etc., is homogeneous too. The idea behind the use of homogeneous source is that an extended geological body causing a potential field anomaly may be replaced by a small number of equivalent point sources whose homogeneity depends on the shape of the geological source. The equivalent sources associated with an extended body will depend on the scale (i.e., the dilation a) of analysis: at small scales the equivalent sources will be localized on the edges

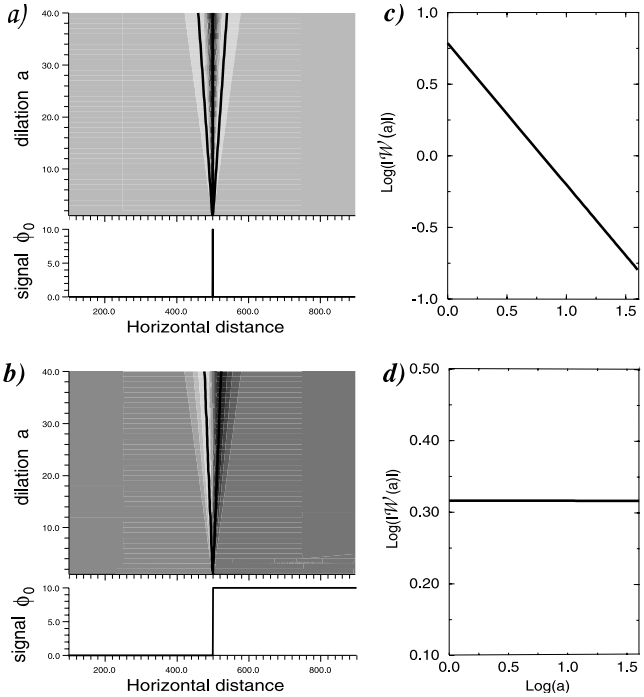

Figure 2. Examples of wavelet transforms of homogeneous singularities of degree (a) $\alpha = -1$ and (c) $\alpha = 0$. The analyzing wavelet is shown in Figure 1b ($\gamma = 2$). Both wavelet transforms have a conspicuous cone-like appearance with an apex pointing onto the location (i.e., the homogeneity center) of the singularity. (b, d) When taken along any ridge of the cone, the amplitude of the wavelet transform varies according to a power law of exponent α.

of the geological source, and at large scales the equivalent sources will be more global as discussed in details by *Sailhac and Gibert* [2003]. Assuming homogeneous causative sources, when upward continued at a level $z_0 + \Delta z$, the potential field is simply a dilated, and of course a rescaled, version of the potential field measured at a reference level z_0 above the source. This behavior is very similar to what is described by equation (8) with the additional property that the altitude offset Δz is equivalent to the dilation a. A modified version of equation (11) may be obtained if the analyzing wavelet g belongs to the so-called Poisson wavelet family which are potential field anomalies caused by homogeneous sources and for which the dilation a also corresponds to and upward continuation offset Δz. *Moreau et al.* [1997, 1999] demonstrated that this family may be generated by applying homogeneous Fourier multipliers of arbitrary degree $\gamma \geq 1$ to the Poisson semigroup kernel p which, in 1-D, reads

$$p(x) = \frac{c_1}{1 + |x|^2}, \tag{12}$$

where c_1 is a normalizing constant. From the point of view of potential field theory [e.g., *Blakely*, 1996], the Fourier multiplier is equivalent to computing vertical, horizontal or oblique derivatives from which more sophisticated operators like reduction to the pole may be derived [*Gibert and Galdéano*, 1985]. Hence, by using the Poisson wavelets, the dilation $a = \Delta z$, and the wavelet transform is the upward continued and derivated potential field ϕ_0 measured at z_0. The same physical reasoning was also followed by *Hornby et al.* [1999], who independently obtained results similar to ours.

[12] If the analyzing wavelet g belongs to the Poisson family, the wavelet transform of a potential field ϕ_0 measured at level $z_0 = 0$ and created by a homogeneous source satisfies [*Moreau et al.*, 1999],

$$\mathcal{W}[g, \phi_0](b, a) = \left(\frac{a}{a'}\right)^{\gamma} \left(\frac{a' - z_\sigma}{a - z_\sigma}\right)^{\gamma-\alpha-2} \mathcal{W}[g, \phi_0]\left(b\frac{a' + z_\sigma}{a + z_\sigma}, a'\right), \tag{13}$$

where α is the homogeneity degree (see equation (9)) of the source located at a depth z_σ.

[13] This expression is similar to (11) except for the z_σ term present in the right-hand side. For instance, and contrary to what happens for equation (11) for which the cone-like pattern converges on the line $a = 0$ (Figure 2), the $b(a' + z_\sigma)/(a + z_\sigma)$ term present in equation (13) brings a fundamental difference in the sense that the cone-like pattern now converges toward an apex located in the negative-dilation domain on the line $a = z_\sigma$.

[14] By applying the following rescaling,

$$\mathcal{W}[g, \phi_0](b, a) \longrightarrow \left(\frac{1}{a}\right)^{\gamma} \mathcal{W}[g, \phi_0](b, a), \tag{14}$$

and a change of coordinates along the dilation axis,

$$a \longrightarrow a - z_\sigma, \tag{15}$$

equation (13) can be rewritten under a form similar to (11),

$$\mathcal{W}[g, \phi_0](b, a') = \left(\frac{a'}{a}\right)^{-\gamma+\alpha+2} \mathcal{D}_{a'/a} \mathcal{W}[g, \phi_0](b, a). \tag{16}$$

In a way very similar to that which can be done for homogeneous functions, the wavelet transform then allows for a straightforward determination of the regularity α of the source causing the analyzed potential field.

2.3. The 2-D Continuous Ridgelet Transform

[15] The 1-D wavelet method presented in the preceding sections formally applies to 2-D potential field anomalies invariant in the y horizontal direction perpendicular to x. Such anomalies are produced by sources infinitely elongated in the y direction.

[16] Let us now consider the case of a 2-D potential field anomaly $\phi_0(\mathbf{h})$ measured in the horizontal plane $z = z_0$ whose point coordinates are represented by the horizontal vector $\mathbf{h}$. Assuming that the anomaly is elongated in a direction represented by the unit vector $\mathbf{s}_\parallel$, the x direction is chosen perpendicular to $\mathbf{s}_\parallel$, and the coordinate $x = \mathbf{h} \cdot \mathbf{s}_\perp$ where $\mathbf{s}_\perp$ is a unit vector perpendicular to the anomaly strike $\mathbf{s}_\parallel$. Accordingly, the $y = \mathbf{h} \cdot \mathbf{s}_\parallel$ coordinate is taken parallel to $\mathbf{s}_\parallel$. With these 2-D notations, the 1-D wavelet transform given by equation (6) may be generalized to give the

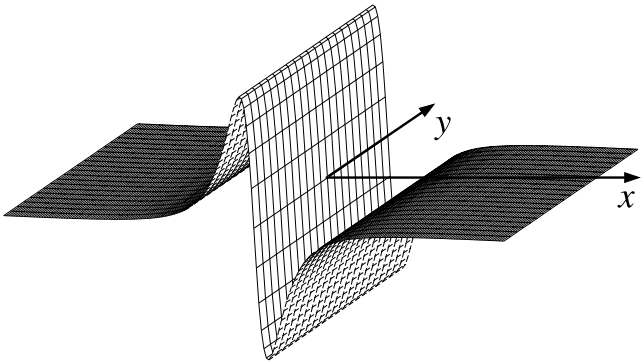

Figure 3. Example of analyzing ridgelet obtained by using the wavelet g shown in Figure 1a in equation (18).

ridgelet transform [*Candès*, 1998; *Candès and Donoho*, 1999],

$$\mathcal{R}[r,\phi_0](b,a,\mathbf{s}_\perp) = \int_{\mathrm{R}^2} \frac{1}{a} r\left(\frac{b-x}{a}, y, \mathbf{s}_\perp\right)\phi_0(x,y)\mathrm{d}x\mathrm{d}y, \quad (17)$$

where the 2-D analyzing ridgelet is obtained by steering a 1-D Poisson wavelet $g(x)$ in the perpendicular direction y,

$$r(b-x,y,\mathbf{s}_\perp) = g(b-\mathbf{h}\cdot\mathbf{s}_\perp)\times 1(y). \quad (18)$$

A ridgelet r is then a 2-D function invariant in the $\mathbf{s}_\parallel$ direction and equals to $g(x)$ in the $\mathbf{s}_\perp$ direction (Figure 3) [*Candès*, 1998]. The unity function $1(y)$ is used in equation (18) to emphasize the y-dependence of the ridgelets. Observe that the ridgelet transform depends on the variable $\mathbf{s}_\perp$. Using the definition of equations (6) and (18), equation (17) may be rewritten by splitting the double integral as

$$\mathcal{R}[r,\phi_0](b,a,\mathbf{s}_\perp) = \int_{\mathrm{R}} \frac{\mathrm{d}x}{a} g\left(\frac{b-x}{a}\right)\int_{\mathrm{R}}\phi_0(x,y)\mathrm{d}y \quad (19)$$

$$= \mathcal{W}\left[g,\mathcal{RT}\left[\phi_0,\mathbf{s}_\parallel\right]\right](b,a), \quad (20)$$

where we have introduced the Radon transform, $\mathcal{RT}$, of the potential field anomaly,

$$\mathcal{RT}\left[\phi_0,x,\mathbf{s}_\parallel\right] \equiv \int_{\mathrm{R}}\phi_0(x,y)\mathrm{d}y. \quad (21)$$

The explicit dependence of the Radon transform with respect to $\mathbf{s}_\parallel$ is here to recall that the y-integration is done along the strike direction.

[17] Equation (20) shows that the ridgelet transform of elongated quasi-2-D anomalies is given by the 1-D wavelet transform applied in the Radon domain. In practice, this is done by computing a 1-D wavelet transform for each direction in the Radon domain. In the next section, we consider the practical issues related to the application of equation (20).

3. Practical Issues

[18] In this section, we address the practical issues pertaining to the application of the Poisson ridgelet transform to the analysis of potential field anomalies. In order to make the explanations clearer, we illustrate this section by applying the method to a synthetic magnetic map consisting in the anomalies of three vertical prismatic bodies with different center positions (x_c, z_c), sizes, depths to top, thicknesses, and magnetization intensities $|\mathbf{J}|$. The values chosen for these parameters are listed in Table 1, and the directions of both the normal field and the magnetization are taken vertical. The magnetic anomalies produced by this model were computed according to the formula of *Bhattacharyya* [1964] and are shown in Figure 4. The effects of noise are identical to those observed for the 1-D wavelet analysis, and they have already been discussed in detail in previous studies [*Moreau et al.*, 1997, 1999; *Sailhac et al.*, 2000; *Sailhac and Gibert*, 2003].

3.1. Computing the Radon Transform

[19] The first stage of the ridgelet analysis consists in computing the Radon transform given by equation (21). In order to make the analyzing ridgelet admissible and the integral of equation (21) finite, it is necessary to give a limited support, $\mathcal{S}_y$, of length L_y to $r(\mathbf{h})$ in the strike direction. Hence the integrals in equation (19) are actually limited to a rectangular domain $\mathcal{S} = \mathcal{S}_x \times \mathcal{S}_y$ forming the support of the ridgelet. In practice, as discussed below, the choice of the domain $\mathcal{S}$ of size $L_x \times L_y$ is not particularly difficult and must such that $\mathcal{S}$ contains the whole analyzed anomaly. The transverse size L_x must be sufficiently large to allow the computation of the wavelet transform over a significant dilation range, and we observed that a good choice is when L_x roughly equals the depth of the source causing the analyzed anomaly. Of course this condition can only be a posteriori verified when the whole analysis procedure is accomplished. Accounting for these adjustments, the modified version of the ridgelet transform actually used in the remaining of this study reads

$$\mathcal{R}[r,\phi_0](b,a,\mathbf{s}_\perp) = \int_{\mathcal{S}_x}\frac{\mathrm{d}x}{a} g\left(\frac{b-x}{a}\right)\mathcal{RT}_{sn}\left[\phi_0,x,\mathbf{s}_\parallel\right], \quad (22)$$

Table 1. Parameters of the Prismatic Bodies Used to Produce the Anomaly Map Shown in Figure 4[a]

Prism	x_c	y_c	Length	Width	Angle	Depth	Thickness	**J**
A	70	90	100	2	40	2.	0.5	3
B	60	35	90	2	−20	4.	0.5	−3
C	95	80	200	2	120	6	12.0	1

[a]Magnetization **J** of the prisms and the normal field are vertical. All distances are given in kilometers, the angles are in degrees from the x direction (i.e., horizontal axis in Figure 4), and the magnetization is given in Am^{-1} (positive downward and negative upward). See text for definitions of symbols.

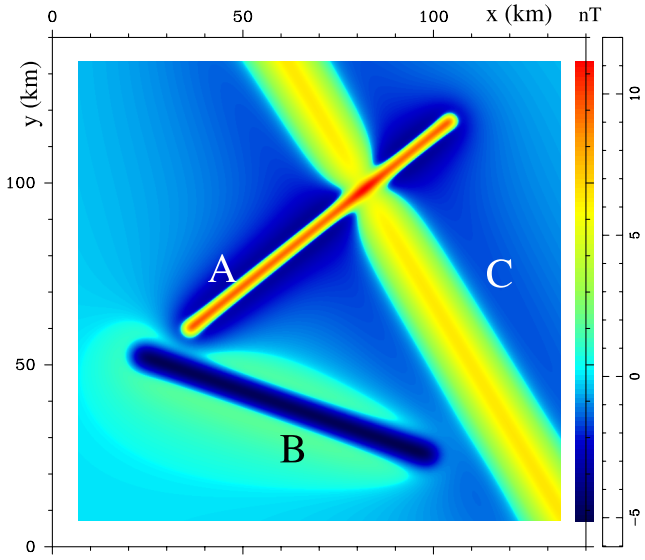

Figure 4. Synthetic anomaly map of the total magnetic field produced by three prismatic bodies whose parameters are given in Table 1.

where the seminormalized Radon transform, $\mathcal{RT}$ of the potential field anomaly is used,

$$\mathcal{RT}_{sn}[\phi_0, x, \mathbf{s}_{\|}] \equiv \frac{1}{L_y} \int_{\mathcal{S}_y} \phi_0(x, y) \mathrm{d}y. \tag{23}$$

[20] In the present study we compute the Radon transform (23) through a direct integration of the anomaly map along each line $b - \mathbf{h} \cdot \mathbf{s}_{\perp} = x$ instead of working in the Fourier domain [e.g., *Bracewell*, 1978] where ghost images of the anomalies appear because of the implicit periodization of the transformed map. The range spanned by the x coordinate equals the size L_x of the analyzed subdomain $\mathcal{S}$; that is, the integration is not done in the four corners of $\mathcal{S}$ where the amount of data is too small to obtain a significant integration. The integration is done by finely interpolating the anomaly map along each line. Because of the intrinsic smooth nature of potential fields the interpolation is not particularly difficult to handle, and we used the algorithm of *Akima* [1974] which supposes data sampled onto a rectangular grid with meshes of possibly variable size. A more rapid method would be to use the so-called recto-polar approximation [*Starck et al.*, 2002], but this method proved to be less accurate and also does not allow a fine and arbitrary sampling along the angular axis of the Radon transform.

[21] The Radon transform of the anomaly map shown in Figure 4 is represented in Figure 5. In the present instance, the domain $\mathcal{S}$ was defined as the whole anomaly map. The horizontal axis corresponds to the position x of the integration lines, and the vertical axis corresponds to the angular direction, θ_r, of the lines, i.e., to the y direction. Let us recall that the x coordinate corresponds to the axis perpendicular to the integration lines of a given direction (see Figure 3). In the present study, we place the origin of the x axis at the center of $\mathcal{S}$. Because of obvious symmetry, the angular-direction axis is limited to the $0 \leq \theta_r \leq \pi$.

3.2. Complex Ridgelet Transform

[22] Once in the Radon domain, the ridgelet transform becomes a series of 1-D wavelet transforms, and in the present study we use the complex analyzing wavelets introduced by *Sailhac et al.* [2000] and *Boukerbout et al.* [2003]. These wavelets are such that their imaginary part is the Hilbert transform of their real part; that is, the wavelets are analytic signals whose envelope (i.e., modulus) and phase may be computed.

[23] Both the modulus and the phase of the ridgelet transforms of the three anomalies of Figure 4 are shown in Figure 6. In the examples, the analyzing wavelet has $\gamma = 1$ and its real part is shown in Figure 3. The ridgelet transforms corresponding to anomalies *A*, *B*, and *C* in Figure 4 have been computed at the respective angular positions 40°, 160°, and 120° in the Radon domain and represented by three horizontal lines in Figure 5. In practice, the choice of these angular positions is interactively done in order to easily localize where the Radon transform locally takes its maximum peak-to-peak amplitude. The signals shown below each ridgelet transform in Figure 6 are actually the Radon transform taken along horizontal lines at the chosen angular positions.

[24] As can be observed, both the modulus and the phase of the ridgelet transforms display conspicuous cone-like signatures associated with each analyzed anomaly. The strong decrease of the modulus observed as dilation increases is caused by the upward continuation property of the analyzing Poisson wavelet. The occurrence of conical signatures indicates that the anomalies present in the ana-

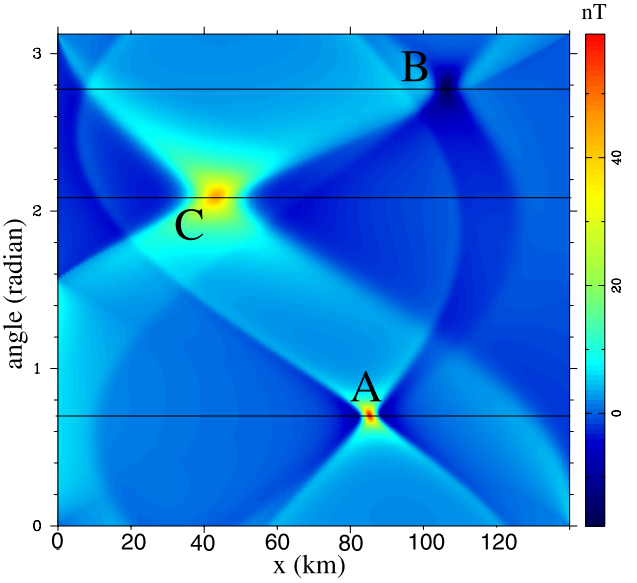

Figure 5. Radon transform of the anomaly map shown in Figure 4. The letters identify the signatures of the three magnetic anomalies of Figure 4. The three horizontal lines represent the Radon anomalies analyzed in Figure 6.

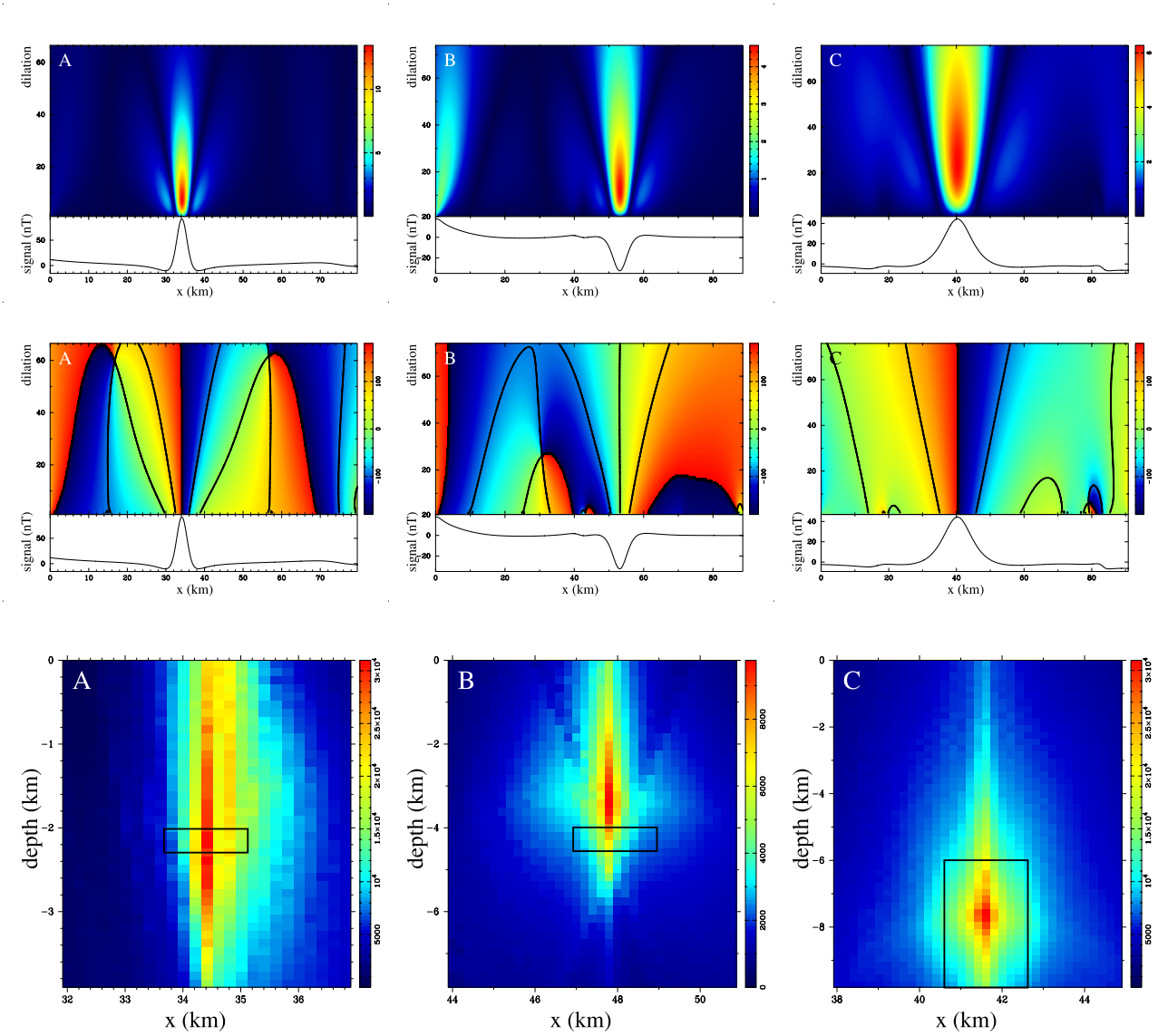

Figure 6. (top) Modulus of the ridgelet transforms of the anomalies shown in Figure 4 (sections A, B, and C are for anomalies A, B, and C, respectively) and corresponding to the three horizontal lines in Figure 5. (middle) Phase of the ridgelet transforms, with values given in degrees and contour line interval equal to $\pi/2$. A conspicuous conical pattern is visible above each anomaly in both the modulus and the phase maps. Half-conical patterns visible at some extremities of the maps are created by edge effects. (bottom) Maps of the entropy criterion (24) obtained for the phase of the ridgelet transforms. The locations of the sources correspond to the maximum values (in red) of the entropy criterion given in equation (24), and the rectangles (solid lines) depict the edges of the initial sources.

lyzed signals may be generated by point sources with a, possibly nonintegral, homogeneity degree.

3.3. Determination of the Source Depth

[25] The ridgelet transforms of Figure 6 are actually 1*D* wavelet transforms, and they display a conspicuous cone-like pattern typical of homogeneous sources [e.g., *Moreau et al.*, 1997, 1999; *Sailhac et al.*, 2000; *Sailhac and Gibert*, 2003; *Boukerbout et al.*, 2003]. As explained in a previous section, the apex of the cone is located below the $a = 0$ horizontal axis of the ridgelet transforms, i.e., at a negative dilation corresponding to the depth of the homogeneous causative source. The determination of the position of the apex may be done either with the modulus or the phase of the ridgelet transform; however, the phase furnishes a more accurate localization because of both its more abrupt variations and also because the conical signature of the sources may directly be processed without performing the rescaling with formulas (14) and (15) [*Boukerbout et al.*, 2003].

[26] In practice, the source depth is determined by scanning the negative-dilation axis and, for each tested depth z_s, the x axis of the ridgelet transform is scanned in order to detect if a location x_s exists where a cone apex is present at $a = -z_s$. The likelihood, ρ, for the occurrence of an apex at

(x_s, z_s) is evaluated with the following criterion [*Tass et al.*, 1998; *Boukerbout et al.*, 2003]:

$$\rho(x_s, z_s) \equiv \frac{\ln N + \sum_{i=1}^{N} h_i \ln h_i}{\ln N}, \qquad (24)$$

where the h_i's are the values of the normalized histogram of either the slopes of the modulus or the phases taken along lines belonging to the cone and diverging from the tested apex.

[27] The bottom part of Figure 6 shows the localization of sources *A*, *B* and *C* (Figure 4) obtained by using their conical signature in the phase of the ridgelet transforms shown above. As can be observed in this figure, all sources are correctly localized both horizontally and vertically. A small vertical bias is observed for source *B* and may be due to slight distortions of the wavelet transform caused by the nearby low-amplitude anomaly centered at x = 40 km and related to interferences with anomaly *A*. Only the shallowest secondary multipolar sources created on the edges of source *C* by the transformation operators acting through the ridgelet analysis ($\partial/\partial z$ in the present example) produce a significant signal. The contribution of the deeper part of *C* to the total anomaly is far weaker and this explains why the homogeneous source localized from anomaly *C* corresponds to the top part of the actual source. As for anomaly *B*, the depth of anomaly *C* may also be slightly biased by the presence of anomaly *B*.

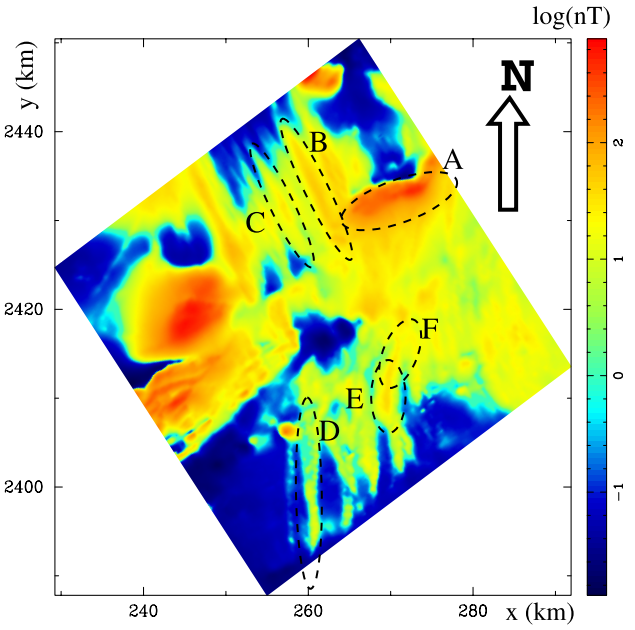

Figure 7. Aeromagnetic map of the Saint Malo region. Labeled areas indicate anomalies analyzed in the present study (see Figure 8). Coordinate system is Lambert France *II* and color scale is linear in the signed $\log_{10}$ of magnetic field. The flight altitude is 350 m above sea level.

4. Application to Aeromagnetic Data

4.1. Aeromagnetic Survey of Northern Britanny

[28] In this section we apply the ridgelet analysis to a part of the aeromagnetic map of the northern Armorican region in Brittany (France). Geological and tectonic studies concerning this region may be found in papers by *Chantraine et al.* [1988], *Brun and Bale* [1990], and *Chantraine et al.* [2001]. The main geodynamic event of this region was a subduction leading to the closure of the Celtic ocean. A high-temperature belt (Guingamp - Saint Malo) formed during the Cadomian orogeny (late Precambrian 600–540 Ma) and obduction of a back-arc basin over a continental margin occurred [*Brun and Bale*, 1990]. The belt is made of micaschists, paragneisses, and migmatites.

[29] The aeromagnetic measurements were done along flight lines 500 m apart, oriented 48°N and at an altitude of 350 m. These data were subsequently interpolated onto a north-south oriented regular grid with a 250 × 250 m mesh and reduced to the pole [*Galdéano et al.*, 2001]. The part of the magnetic map analyzed in the present study is located in the south and eastern part of the Saint Malo Gulf (Figure 7). This region of the aeromagnetic survey of Northern Britanny was previously studied by *Mikhailov et al.* [2003], who performed an Euler deconvolution analysis to localize the magnetic sources associated with elongated magnetic anomalies correlated with a swarm of doleritic dikes (see *Vidal* [1980], *Perroud et al.* [1986], and *Lahaye et al.* [1995] for details). The dikes apparent onshore have an average thickness of 5 m and their associated magnetic anomalies are considerably wider indicating that the emerging narrow dikes are probably connected to wider and deeper magmatic bodies which actually constitute the causative sources of the observed magnetic anomalies. The magnetic anomalies of the Saint Malo region are quasilinear and north-south oriented. Northward, in the Gulf of Saint Malo, their strike changes to northwest-southeast, i.e., roughly parallel to the flight lines of the aeromagnetic survey, and *Galdéano et al.* [2001] carefully discuss and eliminate the possibility that these anomalies could result from incomplete reduction and/or leveling of the magnetic data. The relationship of these anomalies with the Guingamp Saint Malo belt is unclear, since the structure of the magnetic anomalies close to their intersection is complicated.

4.2. Source Location by Ridgelet Analysis

[30] We apply the ridgelet analysis to 6 magnetic anomalies labeled from *A* to *F* in Figure 7, and representative of the causative sources expected in this region. Anomaly *A* corresponds to anomaly 2 in Figure 6 of *Mikhailov et al.* [2003] and is probably associated with an intrusive body emplaced after the dikes. Anomalies *B*, *C*, *D* and *E* are associated with doleritic dikes. Anomaly *F* has a different orientation and its association with a dike is less clear.

[31] The locations of the sources associated with the six selected anomalies are shown in Figure 8. As can be observed the entropy criterion has a rather sharp maximum both in the horizontal and the vertical directions. This results in a very good localization of the sources. Several source localizations have been performed with the Euler deconvolution method [*Asfirane and Galdéano*, 2000; *Mikhailov et al.*, 2003], and a comparison with the results obtained by *Mikhailov et al.* [2003] shows that the ridgelet depths are in very good agreement with the Euler depths

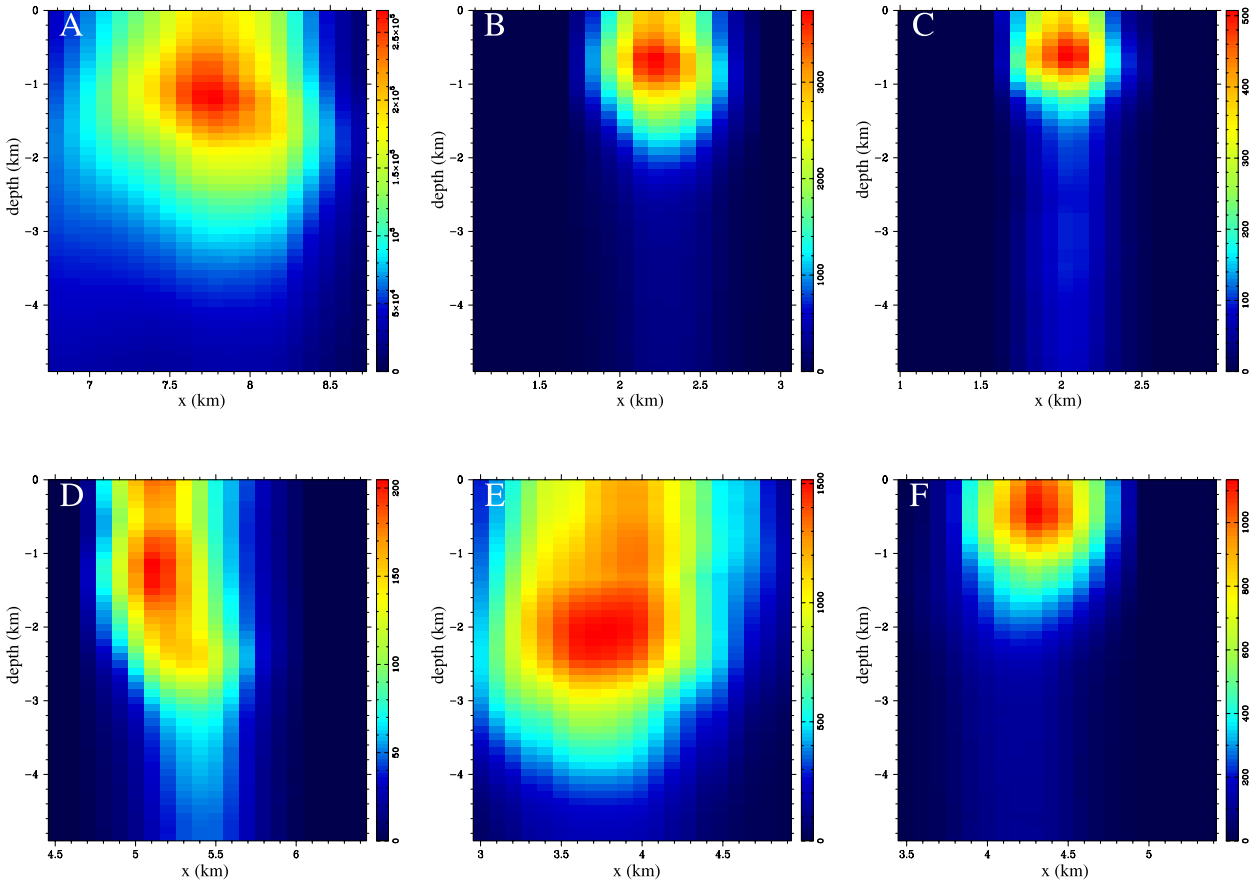

Figure 8. View of the sources located by ridgelet analysis of the magnetic anomalies shown in Figure 7. Depth are given relative to the flight altitude (i.e., 350 m above sea level).

(see Table 2) and provide a sharper determination for large depths than obtained with the Euler method.

5. Conclusion

[32] The synthetic examples presented above illustrate the main steps of the localization of sources of potential field by means of the ridgelet transform based on the Poisson analyzing wavelets. The main step of the method is to bring the information into the Radon domain where elongated anomalies are recognized as localized high-amplitude signatures. The ridgelet analysis is then applied to each selected Radon signature to localize the causative sources of the potential field anomaly. The main advantage of this approach is its capability to automatically decompose a measured anomaly map into elementary anomalies, each being associated with a homogeneous source. This atomic decomposition may be of great help in identifying the causative bodies of measured anomalies and bringing prior information to more sophisticated inversion techniques. Indeed, the decomposition may be considered as optimal in the sense that it involves the smallest as possible number of causative sources. Consequently, the ridgelet analysis gives some indication about the number of independent parameters to be determined if an inverse approach is subsequently used. The ridgelet analysis could then be used to regularized inversion methods which are notoriously known to be ill-posed. A similar approach has recently been followed by *Li and Oldenburg* [2003], who used orthogonal wavelets and thresholding [e.g., *Moreau et al.*, 1996] to reduce the number of parameters to be inverted.

[33] In the present study, the ridgelet analysis is implemented in an interactive way and the user may easily define the subareas containing selected anomalies map for which a local ridgelet analysis is desired. The user may also select the relevant angles in the Radon transform, i.e., corresponding to the strikes of the elongated anomalies present in the analyzed map. The last interactive step of

Table 2. Ridgelet Depths Obtained in the Present Study (See Figure 8) and Euler Depths Derived by *Mikhailov et al.* [2003] for the Six Selected Anomalies Shown in Figure 7[a]

Anomaly	Depth Derived in the Present Study, km	Depth Derived by *Mikhailov et al.* [2003], km
A	0.4–1.0	0.6–5.0
B	0.3–0.6	0.6–0.8
C	0.0–0.4	0.0–0.5
D	0.5–1.2	0.3–0.5
E	1.3–2.1	0.6–5.0
F	0.0–0.3	0.0–0.5

[a]Depths are given relative to the ground level.

the analysis consists in selecting the region of the ridgelet transform containing the conical signature used to compute the entropic criterion from which the source location is determined.

[34] If the causative sources are elongated with a depth varying along strike, it is possible to make a sequence of local analysis in order to track the variable depth of the source body. This is illustrated by both anomalies *E* and *F* (Figure 7) whose local analysis reveal significantly different depths (Figure 8). However, the method ceases to be accurate if the source is so inclined that the depth cannot be considered as constant even in the sub-areas of the local ridgelet analysis. Curved anomalies may equally be processed through a local ridgelet analysis where the initial curved anomaly is decomposed into a small number of straight subanomalies.

[35] **Acknowledgments.** We thank Armand Galdéano who kindly provided the aeromagnetic data of the Saint Malo region. Pascal Sailhac and Erwan Thébault made very detailed and constructive reviews. This paper benefited from discussions with our colleagues Jean-Pierre Brun and Denis Gapais.

References

Akima, H. (1974), A method of bivariate interpolation and smooth surface fitting based on local procedure, *Commun. ACM*, *17*, 18–20.

Alexandrescu, M., D. Gibert, G. Hulot, J.-L. Le Mouël, and G. Saracco (1995), Detection of geomagnetic jerks using wavelet analysis, *J. Geophys. Res.*, *100*, 12,557–12,572.

Alexandrescu, M., D. Gibert, G. Hulot, J.-L. Le Mouël, and G. Saracco (1996), Worldwide wavelet analysis of geomagnetic jerks, *J. Geophys. Res.*, *101*, 21,975–21,994.

Asfirane, F., and A. Galdéano (2000), L'utilisation de la déconvolution d'Euler et du signal analytique pour la localisation des sources magnétiques, *Bull. Soc. Géol. Fr.*, *171*, 71–81.

Baranov, W. (1975), *Potential Fields and Their Transformations in Applied Geophysics*, *Geoexplor. Monogr. Ser.*, vol. 6, 121 pp., Gebruder Borntraeger, Stuttgart, Germany.

Bhattacharyya, B. K. (1964), Magnetic anomalies due to prism-shaped bodies with arbitrary polarization, *Geophysics*, *29*, 517–531.

Bhattacharyya, B. K. (1972), Design of spatial filters and their application to high-resolution aeromagnetic data, *Geophysics*, *37*, 68–91.

Blakely, R. J. (1996), *Potential Theory in Gravity and Magnetic Applications*, 441 pp., Cambridge Univ. Press, New York.

Bosch, M., A. Guillen, and P. Ledru (2001), Lithologic tomography: An application to geophysical data from the Cadomian belt of northern Brittany, France, *Tectonophysics*, *331*, 197–227.

Boschetti, F., V. Therond, and P. Hornby (2004), Feature removal and isolation in potential field data, *Geophys. J. Int.*, *159*, 833–841, doi:10.1111/j1365-246X.2004.02293.x.

Boukerbout, H., D. Gibert, and P. Sailhac (2003), Identification of sources of potential fields with the continuous wavelet transform: Application to VLF data, *Geophys. Res. Lett.*, *30*(8), 1427, doi:10.1029/2003GL016884.

Bracewell, R. (1978), *The Fourier transform and its Applications*, McGraw-Hill, New York.

Brun, J. P., and P. Bale (1990), Cadomian tectonics in northern Brittany, *Geol. Soc. Spec. Publ.*, *51*, 95–114.

Candès, M. (1998), *Ridgelets: Theory and Applications*, Ph.D. thesis, Dep. of Stat., Stanford Univ., Stanford, Calif.

Candès, M., and D. L. Donoho (1999), Ridgelets: A key to higher-dimensional intermittency?, *Philos. Trans. R. Soc., Ser. A*, *357*, 2495–2509.

Chantraine, J., J.-J. Chauvel, P. Bale, E. Denis, and D. Rabu (1988), Le Briovérien (Protérozoique supérieur à terminal) et l'orogénèse cadomienne en Bretagne (France), *Bull. Geol. Soc. Fr.*, *4*, 815–829.

Chantraine, J., E. Egal, D. Thieblemont, E. Le Goff, C. Guerrot, M. Ballévre, and P. Guennoc (2001), The Cadomian active margin (North Armorican massif, France): A segment of the North Atlantic Panafrican belt, *Tectonophysics*, *331*, 1–18.

Cuer, M., and R. Bayer (1980), Fortran routines for linear inverse problems, *Geophysics*, *45*, 1706–1719.

Dobrin, M. B., and C. H. Savit (1988), *Introduction to Geophysical Prospecting*, 4th ed., McGraw-Hill, New York.

Fedi, M., R. Primiceri, T. Quarta, and A. V. Villani (2004), Joint application of continuous and discrete wavelet transform on gravity data to identify shallow and deep sources, *Geophys. J. Int.*, *156*, 7–21, doi:10.1111/j1365-246X.2004.02118.x.

Galdéano, A. (1974), *Traitement des données aéromagnétiques: Méthodes et applications*, Ph.D. thesis, 153 pp., Univ. Pierre et Marie Curie, Paris.

Galdéano, A., F. Asfirane, C. Truffert, E. Egal, and N. Debeglia (2001), The aeromagnetic map of the French Cadomian belt, *Tectonophysics*, *331*, 99–108.

Gibert, D., and A. Galdéano (1985), A computer program to perform transformations of gravimetric and aeromagnetic surveys, *Comput. Geosci.*, *11*, 553–588.

Gibert, D., and M. Pessel (2001), Identification of sources of potential fields with the continuous wavelet transform: Application to self-potential profiles, *Geophys. Res. Lett.*, *28*, 1863–1866.

Goupillaud, P., A. Grossmann, and J. Morlet (1984), Cycle-octave and related transforms in seismic signal analysis, *Geoexploration*, *23*, 85–102.

Green, A. G. (1972), Magnetic profile analysis, *Geophys. J. R. Astron. Soc.*, *30*, 393–403.

Grossmann, A., M. Holschneider, R. Kronland-Martinet, and J. Morlet (1987), Detection of abrupt changes in sound signals with the help of wavelet transforms, in *Advances in Electronics and Electron Physics*, vol. 19, pp. 289–306, Elsevier, New York.

Holschneider, M. (1988), On the wavelet transformation of fractal objects, *J. Stat. Phys.*, *50*, 953–993.

Holschneider, M. (1995), *Wavelets: An Analysis Tool*, 423 pp., Clarendon, Oxford, U. K.

Hornby, P., F. Boschetti, and F. G. Horovitz (1999), Analysis of potential field data in the wavelet domain, *Geophys. J. Int.*, *137*, 175–196.

Lahaye, Y., S. Blais, B. Auvray, and G. Ruffet (1995), Le volcanisme fissural paléozoique du domaine nord-armoricain, *Bull. Soc. Géol. Fr.*, *166*, 601–612.

Le Gonidec, Y., D. Gibert, and J.-N. Proust (2002), Multiscale analysis of waves reflected by complex interfaces: Basic principles and experiments, *J. Geophys. Res.*, *107*(B9), 2184, doi:10.1029/2001JB000558.

Le Gonidec, Y., F. Conil, and D. Gibert (2003), The wavelet response as a multiscale NDT method, *Ultrasonics*, *41*, 487–497.

Li, Y., and D. W. Oldenburg (1996), 3-D inversion of magnetic data, *Geophysics*, *61*, 394–408.

Li, Y., and D. W. Oldenburg (2003), Fast inversion of large-scale magnetic data using wavelet transforms and a logarithmic barrier method, *Geophys. J. Int.*, *152*, 251–265.

Mallat, S., and W. L. Hwang (1992), Singularity detection and processing with wavelets, *IEEE Trans. Inf. Theory*, *38*, 617–643.

Martelet, G., P. Sailhac, F. Moreau, and M. Diament (2001), Characterization of geological boundaries using 1-D wavelet transform on gravity data: Theory and application to the Himalayas, *Geophysics*, *66*, 1116–1129.

Mikhailov, V., A. Galdéano, M. Diament, A. Gvishiani, S. Agayan, S. Bogoutdinov, E. Graeva, and P. Sailhac (2003), Application of artificial intelligence for Euler solutions clustering, *Geophysics*, *68*, 168180, doi:10.1190/1.1543204.

Moreau, F., D. Gibert, and G. Saracco (1996), Filtering non-stationary geophysical data with orthogonal wavelets, *Geophys. Res. Lett.*, *23*, 407–410.

Moreau, F., D. Gibert, M. Holschneider, and G. Saracco (1997), Wavelet analysis of potential fields, *Inverse Probl.*, *13*, 165–178.

Moreau, F., D. Gibert, M. Holschneider, and G. Saracco (1999), Identification of sources of potential fields with the continuous wavelet transform: Basic theory, *J. Geophys. Res.*, *104*, 5003–5013.

Negi, J. G. (1967), Convergence and divergence in downward continuation, *Geophysics*, *32*, 867–871.

Parker, R. L. (1994), *Geophysical Inverse Theory*, Princeton Univ. Press, Princeton, N. J.

Paul, M. K., S. Data, and B. Banerjee (1966), Direct interpretation of two-dimensional structural faults from gravity data, *Geophysics*, *31*, 940–948.

Perroud, H., B. Auvray, N. Bonhommet, J. Mace, and R. van Voo (1986), Paleomagnetism and K-Ar dating of Lower Carboniferous dolerites dykes from northern Brittany, *Geophys. J. R. Astron. Soc.*, *87*, 143–153.

Pilkington, M. (1997), 3-D magnetic imaging using conjugate gradients, *Geophysics*, *62*, 1132–1142.

Pilkington, M., M. E. Gregotski, and J. P. Todoeschuck (1994), Using fractal crustal magnetization models in magnetic interpretation, *Geophys. Prospect.*, *42*, 677–692.

Roy, A. (1967), Convergence in downward continuation for some simple geometries, *Geophysics*, *32*, 853–866.

Sailhac, P., and D. Gibert (2003), Identification of sources of potential fields with the continuous wavelet transform: Two-dimensional wavelets and multipolar approximations, *J. Geophys. Res.*, *108*(B5), 2262, doi:10.1029/2002JB002021.

Sailhac, P., and G. Marquis (2001), Analytic potentials for the forward and inverse modeling of SP anomalies caused by subsurface fluid flow, *Geophys. Res. Lett.*, *28*, 1851–1854.

Sailhac, P., A. Galdéano, D. Gibert, F. Moreau, and C. Delor (2000), Identification of sources of potential fields with the continuous wavelet transform: Complex wavelets and applications to magnetic profiles in French Guiana, *J. Geophys. Res.*, *105*, 19,455–19,475.

Sowerbutts, W. T. C. (1987), Magnetic mapping of the Butterton Dyke: An example of detailed geophysical surveying, *J. Geol. Soc.*, *144*, 29–33.

Spector, A., and F. S. Grant (1970), Statistical models for interpreting aeromagnetic data, *Geophysics*, *35*, 293–302.

Starck, J.-L., E. J. Candés, and D. L. Donoho (2002), The curvelet transform for image denoising, *IEEE Trans. Image Process.*, *11*, 670–684.

Tarantola, A. (1987), *Inverse Problem Theory*, Elsevier, New York.

Tass, P., M. G. Rosenblum, J. Weule, J. Kurths, A. Pikovsky, J. Volkmann, A. Schnitzler, and H.-J. Freund (1998), Detection of n:m phase locking from noisy data: Application to magnetoencephalography, *Phys. Rev. Lett.*, *81*, 3291–3294.

Thompson, D. T. (1982), EULDPH: A new technique for making computer-assisted depth estimates from magnetic data, *Geophysics*, *47*, 31–37.

Vidal, P. (1980), L'évolution polyorogénique du Massif Armoricain: Rapport de la géochronologie et de la géochimie isotopique du strontium, *Mem. Soc. Geol. Mineral. Bretagne*, *21*.

H. Boukerbout, Centre de Recherche en Astronomie, Astrophysique & Géophysique, B.P. 63, Bouzareah, 16340 Alger, Algeria.

D. Gibert, Géosciences Rennes, Université Rennes 1, B15 Campus de Beaulieu, F-35042 Rennes, France. (gibert@univ-rennes1.fr)